

# Motion Estimation from Tagged MR Image Sequences

Jerry L. Prince, *Member, IEEE*, and Elliot R. McVeigh

**Abstract**—A method to reconstruct motion from sequences of tagged magnetic resonance (MR) images is presented. MR tagging is used to create a spatial pattern of varying magnetization so that objects which may otherwise have constant intensity are textured, which reduces the motion ambiguity associated with the aperture problem in computer vision. To compensate for the decay of the tag pattern, a new optical flow algorithm is developed and implemented. The resulting estimated velocity field is then used to recursively update the implied motion reference map over time, thereby tracking the motion of individual particles. If a segmentation of the object is known at the time the tag pattern is created, then an object may be selectively tracked, using the estimated reference map to update the object's position as time progresses. Results are shown for both simulated and actual MR phantom data.

## I. INTRODUCTION

**D**ETAILED measurement of cardiac motion is an important goal in medical imaging since motion parameters can be used to indicate abnormal heart function [1]–[3]. In particular, it has been noted that evidence of reduced transmural strain and left-ventricular torsion may both be important indicators of myocardial ischemia [4]–[6]. Although many methods have been proposed to automatically detect the motion of the epicardium and endocardium using echocardiography [7]–[10], motion *within* the myocardium is much more difficult to observe in echocardiograms since these images are dominated by speckle [11]. Transmural motion is also difficult to observe in standard computed tomography (CT) and magnetic resonance (MR) images since there is relatively little image contrast within the myocardium [12], [4]. Thus, the development of new imaging methods to visualize and measure motion within the myocardium has become an important goal in cardiac imaging.

The current “gold standards” in cardiac motion imaging use either implanted metallic (or radiopaque) markers together with X-ray imaging [13], [14], or implanted sonomicrometers [15], [16]. While these techniques are very important in cardiac motion research, they are rarely used clinically because of their extreme invasiveness. Direct MR velocity imaging, originally

invented for imaging blood flow [17], has recently yielded cine velocity images of the heart [18]. However, because of the extra time required to generate the flow-compensation gradient pulses, these images tend to be very sensitive to higher order motion components (such as acceleration) which are prevalent in the heart. Thus, although faster gradient coils will improve this situation in the future, direct velocity images of the heart are currently quite noisy and full of artifacts, especially in oblique planes (which are required for short-axis ventricular images).

MR tagging has recently been introduced for cardiac motion imaging [19]–[21]. In MR tagging, a spatially varying pattern of longitudinal magnetization is encoded in the body prior to each phase-encoded data acquisition cycle of a spin-echo imaging sequence. This pattern is revealed in the complete image as a texture or pattern in the tissue; motion occurring between the tag pulse sequence and the image pulse sequence results in a distortion of the tag pattern. Methods to analyze the motion of the tag pattern have been reported in the literature [22], [23]. These methods, however, match points between images, and therefore give relatively sparse information. In contrast, in this paper we describe an approach based on the methods of optical flow, which provides a motion estimate for each pixel within the image.

Optical flow (OF) is a method for analyzing the motion of pixels between image pairs [24]. It is based on a differential analysis of the images—requiring estimates of both the spatial gradient and spatial time derivative at each pixel—and requires regularization to produce a unique solution. In the approach of Horn and Schunk [24], which we follow closely in this paper, this regularization is provided using a variational approach that includes smoothness of the velocity field as *a priori* knowledge. Application of OF methods to MR tagged images requires an additional modification, however. Since the tag pattern fades away in time (see Section II) the standard assumption used in OF—that the material time derivative of all points within the field-of-view is zero—is violated. Hence, our OF method, which we call *variable brightness optical flow* (VBOF) uses the MR imaging equation for tagged images to provide an estimate of the material time derivative, which can be used for optical flow calculations using a slight modification of the standard OF approach.

Because MR tagging *creates* patterns within the tissue, VBOF can be used to track motion within relatively homogeneous regions such as the myocardium. Thus, motion that may be completely invisible (such as the rotation of a homogeneous disk) can be imaged by this approach. The

Manuscript received July 26, 1991; revised November 22, 1991. This work was supported in part by the National Heart, Lung, and Blood Institute, National Institutes of Health under Grant R01-HL45090. The work of E. R. McVeigh was supported in part by a Radiological Society of North America Scholar's Award.

J. L. Prince is with the Department of Electrical and Computer Engineering, Image Analysis and Communications Laboratory, The Johns Hopkins University, Baltimore, MD 21218.

E. R. McVeigh is with the Department of Biomedical Engineering, Medical Imaging Laboratory, The Johns Hopkins University, Baltimore, MD 21205.

IEEE Log Number 9106789.

problem of measuring motion so obscured has been called the *aperture problem* in the computer vision literature [25], and has been a frequently cited reason against using optical flow in motion analysis from image sequences. Approaches that have used optical flow methods using standard medical imaging modalities where large regions of relatively homogeneous brightness—CT [26] and ultrasound [11]—have been limited by the aperture problem. In fact, the motion of the interior portions of the muscle must be largely inferred from the motion of the nearest walls. Thus, although it is not shown in these papers, it is likely that the rotational component of motion is completely missing. In our approach, however, such global aperture problems are eliminated; only local ambiguity remains (see [25]), and this we have in common with all optical flow methods.

This paper is organized as follows. In Section II we provide models for the MR tagging process and for motion, and in Section III we develop the optical flow and motion-tracking algorithms. Section IV presents experimental results for computer simulations and actual MR data, and Section V provides a conclusion. Parts of this work have been previously reported in conference papers [27]–[29]; this paper, however, contains a complete discourse and presents new results.

## II. MR TAGGING AND MOTION MODELS

Tagged MR images of a slice of the heart at a particular cardiac phase can be obtained using electrocardiographic gating [19]. A timing diagram showing the sequence of events required to obtain the tagged MR images used in this paper is shown in Fig. 1. This pulse sequence is described in detail in Section IV and in Appendixes A and B. At end-diastole (just before contraction starts), the tissues are tagged by selectively tipping the resting spins through angles varying between 0 and  $180^\circ$  in a specific spatial pattern. During one cardiac cycle, a single phase-encoding of a standard spin-echo image is taken. This two-step procedure—a tagging pulse sequence followed by an imaging pulse sequence—is repeated in subsequent cardiac cycles until all the phase-encodings have been obtained. Full 3-D time-sequences are obtained by acquiring different slices using various time intervals between the tagging pulse-sequence and the imaging pulse-sequence.

Each point  $\mathbf{p}$  in the body possesses three parameters that are significant to MR imaging: the longitudinal relaxation time  $T_1$ , the transverse relaxation time  $T_2$ , and the spin density  $D_0$ . The pixel intensities within *tagged* MR images, however, are determined not only by tissue parameters, but also by the initial spatial tag pattern and the motion that occurs between the time the tag pattern is created and the time the image is taken. We assume that the cardiac cycle is perfectly repeating and that as the tissue moves in time, its MR parameters do not change. Therefore, a collection of images obtained over many cardiac cycles by electrocardiographic gating can be viewed as having been obtained in one cardiac cycle (except that the effects of  $T_R$  must be taken into account in the development of the imaging equation). Also, a particle having a unique intensity could, in theory, be tracked through successive images. Unfortunately, without

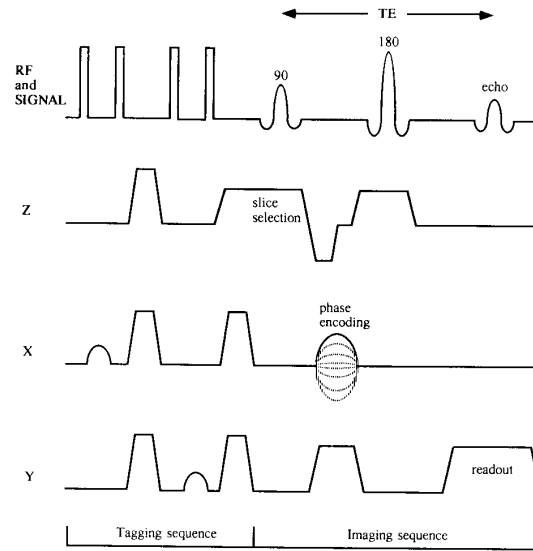


Fig. 1. A pulse-sequence timing diagram for obtaining tagged MR images.

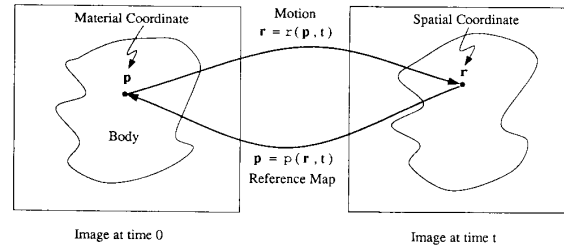


Fig. 2. Relationship between the motion of a material point and the reference map of a spatial coordinate.

tagging, tissues within the myocardium have nearly the same intensity; consequently, tracking motion in this case does not permit both accurate and high-resolution motion estimates. MR tagging, however, allows the introduction of spatial gradients where none may otherwise exist, and both high-resolution and accurate estimates become possible. To capture the behavior of the combined effect of tagging and motion, we introduce a mathematical model of motion taken from the theory of continuum mechanics [30] and a phenomenological model of MR imaging derived using the Bloch equation [31].

A *motion*, as shown in Fig. 2, is a mapping which takes points in the body, called *material points*, and specifies where these points move in time. We write  $\mathbf{r} = \mathbf{r}(\mathbf{p}, t)$  to indicate that material point  $\mathbf{p}$  has moved to spatial coordinate  $\mathbf{r}$  at time  $t$ ; and taking end-diastole to be  $t = 0$ , we set  $\mathbf{p} = \mathbf{r}(\mathbf{p}, 0)$ , for all  $\mathbf{p}$ . There exists an inverse mapping called the *reference map* which gives the material point for each spatial coordinate at any given time (see Fig. 2). Here, we write  $\mathbf{p} = \mathbf{p}(\mathbf{r}, t)$ . Our overall goal is to track the motion of myocardial tissues; determining  $\mathbf{r}(\mathbf{p}, t)$  for all points  $\mathbf{p}$  which fall within the myocardium is an equivalent mathematical statement of this goal.

A tag pulse-sequence, initiated at  $t = 0$ , tips the magnetization vectors between  $0$  and  $180^\circ$  in a prespecified spatial pattern. A spoiler (or crusher) gradient is then used to dephase the magnetization vectors, eliminating any significant signal from the initial pulses. The effect of the tagging is to spatially modulate the magnetization, which partially determines the intensities in a spin-echo image—but this effect is transient since it decays with  $T_1$ . Using the Bloch equation and the assumption that  $T_2 \ll T_R$ , the spin-echo image brightness function  $\psi(\mathbf{r}, t)$  is the sum of an untagged image  $\psi_0(\mathbf{r}, t)$  and an image  $\psi_T(\mathbf{r}, t)$  which is due solely to the tag pulse-sequence (see Appendix A):

$$\psi(\mathbf{r}, t) = \psi_0(\mathbf{r}, t) + \psi_T(\mathbf{r}, t) \quad (1)$$

where

$$\psi_0(\mathbf{r}, t) = D_0(\mathbf{p})e^{-T_E/T_2(\mathbf{p})} \left(1 - e^{-T_R/T_1(\mathbf{p})}\right), \quad (2a)$$

$$\psi_T(\mathbf{r}, t) = D_0(\mathbf{p})e^{-T_E/T_2(\mathbf{p})} (\xi(\mathbf{p}) - 1) \cdot \left(e^{-t/T_1(\mathbf{p})} - e^{-T_R/T_1(\mathbf{p})}\right), \quad (2b)$$

In these equations the material point  $\mathbf{p}$  is defined by the reference map as  $\mathbf{p} = \mathbf{p}(\mathbf{r}, t)$  and the function  $\xi(\mathbf{p})$ , which we call the *spatial tag pattern*, is equal to the cosine of the tip-angle at  $\mathbf{p}$  required to produce the pattern. In the development presented here, we assume a maximum tip-angle of  $90^\circ$  so that  $\xi(\mathbf{p})$  is always in the range of  $0$  to  $1$ . Generation of a specific tagging pattern is discussed in Section IV and in Appendix B.

We refer to (1) as the *MR imaging equation*. It describes the change in image brightness over time as a function of the MR parameters, the motion, and the initial tag pattern. The correct way to interpret (1) is as follows. The coordinates of an arbitrary pixel within an image represent the spatial coordinate  $\mathbf{r}$ . If the reference map  $\mathbf{p}(\mathbf{r}, t)$  were known (or estimated), then the material point  $\mathbf{p}$  that resides at  $\mathbf{r}$  at time  $t$  is also known (or estimated). Then using (1), the brightness of this point is known and more importantly for our purposes in the following section the time rate of change of brightness of that point is also known. A key assumption to being able to use this equation in this way is that both the tag pattern and the MR parameters—that is,  $T_1$ ,  $T_2$ , and  $D_0$ —over the entire field of view at end-diastole must be known. Since we generate the tag pattern ourselves through a tagging pulse-sequence, we know the pattern. Similarly, in the simulation studies and the phantom experiment in this paper we use known and measured MR parameters, respectively. In more general studies, however, such as in vivo cardiac studies, we will have to either measure the MR parameters over the entire end-diastole image (a daunting prospect, at best), measure the parameters over a portion of the myocardium and assume that they are constant over the entire myocardium, or simply assume constant MR parameters that are typical across a large population. The consequences of measuring or approximating the MR parameters must be considered for *in vivo* studies, but is not of primary concern in this paper.

### III. METHODS

#### A. Variable Brightness Optical Flow

Optical flow algorithms use differential techniques to estimate a velocity vector for each point in an image given two images of a scene at different times [24]. Let the partial derivative of brightness holding  $\mathbf{p}$  constant—that is, the material time derivative of brightness—be denoted by  $\dot{\psi}(\mathbf{r}, t)$ . Then the chain rule for differentiation gives [30]

$$\dot{\psi}(\mathbf{r}, t) = \nabla \psi(\mathbf{r}, t) \cdot V(\mathbf{r}, t) + \psi_t(\mathbf{r}, t) \quad (3)$$

where  $\psi_t(\mathbf{r}, t)$  is the spatial time derivative of brightness (which is the partial derivative of brightness holding  $\mathbf{r}$  constant),  $\nabla \psi(\mathbf{r}, t)$  is the spatial brightness gradient, and  $V(\mathbf{r}, t)$  is the spatial velocity field, which we are trying to determine.

In standard optical flow,  $\dot{\psi}(\mathbf{r}, t)$  is assumed to be zero, which implies that as points move through space their brightness remains constant. This assumption is not true in tagged MR images since the brightness component  $\psi_T(\mathbf{r}(\mathbf{p}, t), t)$  may change in time when  $\mathbf{p}$  is held constant. Equation (3) may be put in the form of a standard optical flow equation, however, by defining

$$\tilde{\psi}(\mathbf{r}, t) = \psi_t(\mathbf{r}, t) - \dot{\psi}(\mathbf{r}, t), \quad (4)$$

which leads to the following *variable brightness optical flow equation*:

$$0 = \nabla \psi(\mathbf{r}, t) \cdot V(\mathbf{r}, t) + \tilde{\psi}(\mathbf{r}, t). \quad (5)$$

If, at a given pixel,  $\nabla \psi$  and  $\tilde{\psi}$  are measured or estimated (described below), then (5) gives a single equation, which is linear in  $V$ . Since  $V$  is a two or three dimensional vector, however, the system is underdetermined, which implies that an infinite number of feasible solutions exist. Therefore, some type of regularization must be used in order to guarantee a unique solution.

The optical flow approach due to Horn and Schunk [24], regularizes the problem by assuming that the velocity field is smooth. We now briefly review this approach and note that the only difference between our approach and the original is that we use  $\dot{\psi}$  instead of  $\psi_t$ . Dropping from our notation the explicit spatial dependence and time dependence of the various functions and letting  $\mathbf{r} = (x, y)$ , the spatial velocity field  $V = (u, v)$  is selected to minimize<sup>1</sup>

$$I = \alpha^2 \iint (u_x)^2 + (u_y)^2 + (v_x)^2 + (v_y)^2 dx dy + \iint (\psi_x u + \psi_y v + \tilde{\psi})^2 dx dy \quad (6)$$

where the  $x$  and  $y$  subscripts denote partial derivatives in the  $x$  and  $y$  directions, respectively. The regularization coefficient  $\alpha^2$  provides a tradeoff between the amount of noise in the calculations of the gradient and time derivatives and the expected smoothness of the velocity field. Rougee, Levy, and Willsky [32] make the selection of  $\alpha^2$  a rigorous consequence

<sup>1</sup> We note that, although at this point we restrict our development to two dimensions, everything presented in this paper may be easily extended to three dimensions.

of having modeled both the noise and the velocity as Brownian processes on the plane. In our work,  $\alpha^2$  is chosen empirically.

In order to minimize (6)  $V$  must satisfy the coupled partial differential equations [24]

$$\nabla^2 u = \frac{1}{\alpha^2} \psi_x (\tilde{\psi} + \psi_x u + \psi_y v) \quad (7a)$$

$$\nabla^2 v = \frac{1}{\alpha^2} \psi_y (\tilde{\psi} + \psi_x u + \psi_y v) \quad (7b)$$

where  $\nabla^2$  is the Laplacian operator. To estimate  $V$  we first estimate  $\nabla\psi = (\psi_x, \psi_y)$  and  $\psi_t$  using simple local derivative approximations (see Appendix C). The material derivative  $\tilde{\psi}$  is found using an estimate of the reference map to determine the material point  $\mathbf{p}$  for each spatial point  $\mathbf{r}$  and then differentiating (1) with respect to  $t$ , yielding

$$\dot{\psi}(\mathbf{r}, t) = -\frac{D_0(\mathbf{p})}{T_1(\mathbf{p})} (\xi(\mathbf{p}) - 1) e^{-T_E/T_2(\mathbf{p})} e^{-t/T_1(\mathbf{p})} \quad (8)$$

where  $\mathbf{p} = \hat{\mathbf{p}}(\mathbf{r}, t)$ , an estimate of the reference map (see next section). Finally, we solve (7a) and (7b) numerically using the local relaxation algorithm described in Kuo *et al.* [33], described for this application in Appendix C. We call this approach *variable brightness optical flow* (VBOF).

### B. Motion Tracking

The main difficulty with VBOF is that measurement of  $\dot{\psi}(\mathbf{r}, t)$  requires knowledge of the material derivative of brightness, which in turn requires knowledge of or an estimate of the reference map of the motion. Clearly, knowing the reference map is equivalent to knowing the motion; and since this is what we are trying to find, it appears that there is an unsolvable dilemma here. We resolve this, however, by using past optical flow calculations to provide an estimate of the reference map for the first of two images in the current optical flow calculation. The VBOF calculation then provides an estimate of the motion from the first to the second image and thereby permits an estimate of the reference map for the second image. This procedure can then be repeated in a recursive fashion over the full image sequence. We note that this procedure estimates the motion of points within the body at each time step and thereby tracks the points in the body. In VBOF, however, tracking is not simply a byproduct of the sequence of optical flow calculations; instead it is an inherent part of VBOF itself, since it is required in order to produce an estimate of  $\dot{\psi}$  for input to VBOF.

We now describe our approach to recursive tracking with VBOF, a block diagram of which is shown in Fig. 3. Assume that a sequence of images taken at times  $t = n\tau$ ,  $n = 0, 1, \dots$  is available.<sup>2</sup> Since by arrangement  $\mathbf{p} = \mathbf{r}(\mathbf{p}, 0)$ , the reference map at  $t = 0$  is just  $\mathbf{p} = \mathbf{p}(\mathbf{p}, 0)$ , the identity map. Hence, given the first two images in the sequence, we may estimate the velocity field between them using variable brightness optical flow as described above, yielding  $\hat{V}(\mathbf{r}, 0) = \hat{V}(\mathbf{p}, 0)$ . A simple estimate of the motion at time  $\tau$  is then given by

$$\hat{\mathbf{p}}(\mathbf{p}, \tau) = \mathbf{p} + \tau \hat{V}(\mathbf{p}, 0). \quad (9)$$

<sup>2</sup>The assumption of equal time increments is not necessary, although it simplifies the discussion.

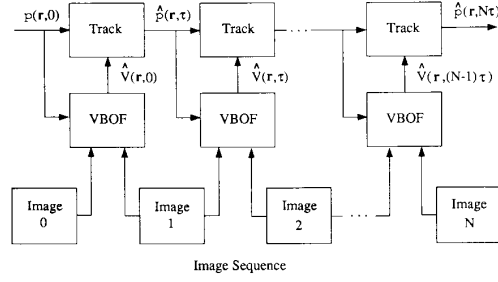


Fig. 3. Recursive motion tracking using variable brightness optical flow (VBOF).

Also, the estimated reference map  $\hat{\mathbf{p}}(\mathbf{r}, \tau)$  at time  $t = \tau$  should satisfy

$$\hat{\mathbf{p}}(\mathbf{r}, \tau) = \mathbf{r} - \tau \hat{V}(\hat{\mathbf{p}}(\mathbf{r}, \tau), 0). \quad (10)$$

Now, assume that at time  $t = n\tau$  reference map estimate  $\hat{\mathbf{p}} = (\mathbf{r}, n\tau)$  is available. To update the estimated reference map at time  $t = (n+1)\tau$  we begin by estimating the velocity field  $\hat{V}(\mathbf{r}, n\tau)$  using VBOF with inputs  $\hat{\mathbf{p}}(\mathbf{r}, n\tau)$ ,  $\psi(\mathbf{r}, n\tau)$ , and  $\psi(\mathbf{r}, (n+1)\tau)$ . Solving

$$\delta p(\mathbf{r}, (n+1)\tau) = \mathbf{r} - \tau \hat{V}(\delta p(\mathbf{r}, (n+1)\tau), n\tau) \quad (11)$$

for  $\delta p(\mathbf{r}, (n+1)\tau)$  provides an incremental reference map estimate  $\delta p(\mathbf{r}, (n+1)\tau)$ , which describes the (inverse) motion between images  $n$  and  $n+1$ . Then the full reference map is estimated using

$$\hat{\mathbf{p}}(\mathbf{r}, (n+1)\tau) = \hat{\mathbf{p}}(\delta p(\mathbf{r}, (n+1)\tau), n\tau). \quad (12)$$

In principle (11) and (12) provide the required recursively updated reference map estimate, the block labeled “Track” in Fig. 3. This update is computationally burdensome as is stated, however. The main problem is that solution of (11) requires knowledge of the displacement leading to a particular pixel’s coordinates at time  $(n+1)\tau$ ; but we do not have this since the previous optical flow calculation gives velocities of the pixels at time  $n\tau$ . If we assume the optical flow algorithm to be symmetric in time, however, then there is a computationally straightforward method to estimate the reference map. Assuming time symmetry implies that given the same two images an optical flow calculation leading to  $\hat{V}(\mathbf{r}, n\tau)$  in the forward time direction would produce the estimate  $-\hat{V}(\mathbf{r}, (n+1)\tau)$  in the backwards time direction. This being the case, it is much more computationally efficient to estimate the reference map (in the forward direction now) using

$$\hat{\mathbf{p}}(\mathbf{r}, (n+1)\tau) = \hat{\mathbf{p}}(\mathbf{r} - \tau \hat{V}(\mathbf{r}, n\tau), n\tau). \quad (13)$$

This calculation requires only a simple interpolation over the lattice, which we do using bilinear interpolation (paying careful attention to the image boundary conditions). Although we use (13) in the simulations presented below, it is not equivalent to (12), since VBOF is not time-reversible (although standard optical flow is time-reversible). This is because our

estimate of  $\dot{\psi}$  applies at the first time only, since this is when we actually have an available motion estimate.

### C. Tracking Objects

The optical flow criterion of (6) imposes a smoothness condition on the underlying velocity field (see [32]) which may be undesirable. For example, when an object moves across a stationary background the velocity field should have a sharp discontinuity at the object's boundary. In this case one would like to allow for such discontinuities as part of the estimation process. In this section, we present an approach to track objects through an image sequence given an initial segmentation, and to "break" the smoothness criterion across object boundaries.

Let  $l(\mathbf{r}, t) \in \{0, 1, 2, \dots, N-1\}$  be an integer label that segments the field-of-view into  $N$  objects. We assume that an initial segmentation of the image is available, and is given by  $l(\mathbf{p}, 0)$ . At a later time, the label of an arbitrary point  $\mathbf{r}$  is estimated using the estimated reference map as

$$\hat{l}(\mathbf{r}, t) = l(\hat{\mathbf{p}}(\mathbf{r}, t), 0). \quad (14)$$

An estimate of the characteristic function of object  $n$  at time  $t$  is then given by

$$\hat{S}_n(t) = \{\mathbf{r} | \hat{l}(\mathbf{r}, t) = n\}. \quad (15)$$

To account for object boundaries, we modify our numerical methods so that local derivatives—that is, the  $x$ ,  $y$ , and  $t$  partial derivatives—are estimated using only pixels with common object labels. Since label estimates are available only for the first of two images in each optical flow calculation, we assume—and this is a possible source of error, especially at or around object boundaries—that the same labels exist within the second image as in the first.

## IV. EXPERIMENTAL RESULTS

Three studies are presented; the first two use simulated data and the third uses phantom data. The first study demonstrates the performance of variable brightness optical flow (VBOF) on image pairs. The second study demonstrates the performance of VBOF combined with tracking applied to image sequences, and the third study demonstrates the performance of the combined algorithm on actual MR data obtained from a rotating phantom.

In both the simulations and the experiments, the spatial tag pattern is given by

$$\xi(\mathbf{p}) = (\cos^2 \theta - \sin^2 \theta \cos k_x p_x)(\cos^2 \theta - \sin^2 \theta \cos k_y p_y). \quad (16)$$

Here,  $k_x$  and  $k_y$  are radial spatial frequencies in the  $x$  and  $y$  directions, respectively,  $\mathbf{p} = (p_x, p_y)$ , and  $\theta = \pi \xi_m / 2$  where  $\xi_m \in [0, 1]$  is a parameter, which we call the *tag modulation coefficient*, controlling the intensity of tag modulation. In experiments involving changes in the spatial frequency of the tag pattern, the coordinate frequencies are reported using the cyclic spatial frequencies  $f_x = k_x / 2\pi$  and  $f_y = k_y / 2\pi$ . The spatial tag pattern in (16) can be generated on an MR

scanner using a spatially modulated magnetization (SPAMM) pulse-sequence as follows (see also [20] and Appendix B). First, a nonselective  $\theta$ -degree RF pulse is generated and followed immediately by a phasing gradient in the  $x$ -direction. Another non-selective  $\theta$ -degree RF pulse is then generated and followed with a spoiler pulse to dephase any remaining transverse magnetization. The integral of the phasing gradient determines the spatial frequency  $k_x$ . This procedure is immediately repeated using the  $y$ -gradient coil and the resulting tag pattern is given in (16). In our phantom experiments, we actually turn on the  $x$  and  $y$  gradients simultaneously, first with positive  $x$  and  $y$  gradients, then with positive  $x$  and negative  $y$  gradients, which causes a  $45^\circ$  rotation of the pattern in (16).

Two error criteria are used in the results described below: average percent velocity error and average tracking error. Average percent velocity error is used to characterize the performance of velocity estimation between image pairs using standard optical flow (SOF) or variable brightness optical flow (VBOF). Given the true velocity  $V = (u, v)$  and an estimate  $\hat{V} = (\hat{u}, \hat{v})$  for a particular pixel, we calculate the percent error as

$$\%Error = 100 \times \frac{1}{2} \left( \frac{|u - \hat{u}|}{u} + \frac{|v - \hat{v}|}{v} \right) \quad (17)$$

where  $|x|$  gives the absolute value of  $x$ . Only pixels that fall within the central portion of the rotating ring phantom are used to calculate the average error that we report. We make this limitation to avoid known artifacts produced at the boundaries of the object.

The tracking error, defined in terms of the true motion and the estimated motion of a particle, is given by

$$\text{Tracking Error} = \|\mathbf{r} - \hat{\mathbf{r}}\| \quad (18)$$

where  $\|\mathbf{x}\|$  gives the euclidean length of  $\mathbf{x}$ ,  $\mathbf{r}$  is the actual motion of  $\mathbf{p}$ , and  $\hat{\mathbf{r}}$  is the estimated motion of  $\mathbf{p}$ . We report this error in pixels, and again, the average is taken only over pixels falling within the central portion of the ring. In all simulations and experiments, the object is labeled and tracked so that derivatives are not computed across object boundaries (see Section III-C). Accordingly, a (true) segmentation of the initial image into the object and its background is provided as input to each algorithm.

The simulated phantom is a ring centered at the origin with inner radius 2.5 cm and outer radius 4.5 cm, digitized onto a 150 by 150 pixel image whose side has length 11.7 cm. The material within the ring has constant  $T_1$ ,  $T_2$ , and  $D_0$ , and the motion is a pure rotation in the counterclockwise direction with frequency of rotation  $f_0$ . The spatial tagging pattern is placed at  $t = 0$  and simulated noise-free images are taken at times  $t = n\tau$  for  $n = 0, 1, \dots, N-1$ . A full sequence of 10 images in which the phantom rotates by approximately  $15^\circ$  is shown in Fig. 4. Note that for this particular object and motion, the motion cannot be observed without tagging.

### A. Study 1: Optical Flow Performance

1) *Effect of Tag Modulation*: In this simulation study, we consider a sequence of just two images and consider the performance of optical flow velocity estimates for different

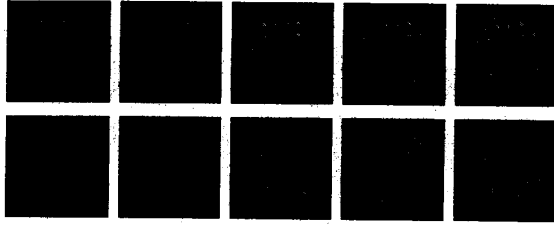


Fig. 4. Proceeding left to right across the top and then the bottom is a simulated tagged MR image sequence for a rotating ring phantom. Here, the spatial frequency of the tag pattern is  $f_x = f_y = 0.75 \text{ cm}^{-1}$ .

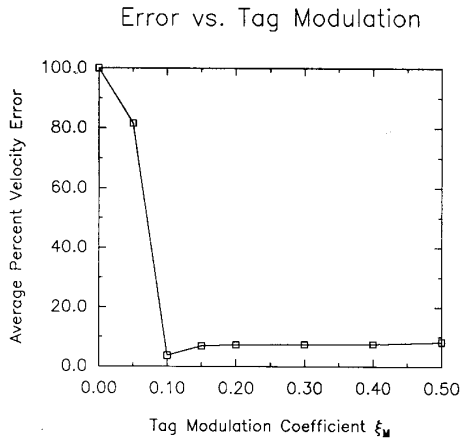


Fig. 5. Optical flow performance as a function of the tag modulation coefficient.

tag modulation coefficients. Here, we make  $T_1$  very large so that there is no difference between VBOF and SOF. As shown in Fig. 5, when there is no tag modulation, i.e.,  $\xi_m = 0.0$ , there is 100% error (indicating, in this case, complete obscurity of motion caused by the aperture effect). The error decreases with increasing  $\xi_m$  up to  $\xi_m = 0.1$  and then gradually increases with increasing  $\xi_m$ . We speculate that this increase is due to the increasing prevalence of near-zero brightness gradients across the tag pattern as  $\xi_m$  increases. This creates velocity ambiguities that are not present in the pattern at  $\xi_m = 0.1$ .

2) *Effect of  $T_1$ :* We now use just two images to compare SOF with VBOF while varying  $T_1$ . Fig. 6 shows a plot of the average percent error in velocity estimation versus  $T_1$  for both algorithms. Clearly, both algorithms degrade with decreasing  $T_1$  (going from right to left in Fig. 6), but SOF does so much more dramatically. The most important observation to make here is that over standard diagnostic ranges of  $T_1$  in heart muscle (from about 0.5 s to 1 s at 1.5 T) the average percent error for VBOF is about 1/10 that of SOF. We conclude that VBOF must be used in place of SOF to track motion in tagged MR images.

To demonstrate the striking difference between the two algorithms, Fig. 7 shows the results of variable OF and standard OF for  $T_1 = 0.5$  s using a needle diagram. In each of these figures, every 5th pixel of the first image of the pair is overlaid with a "needle," indicating the estimated displacement of each

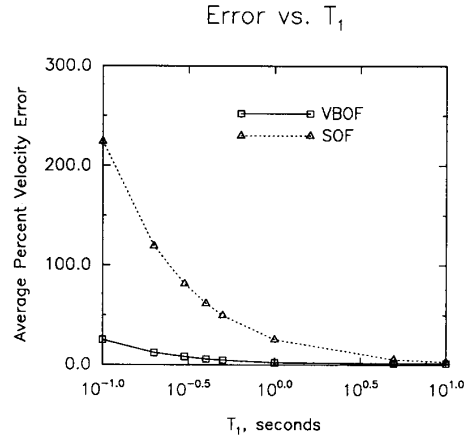


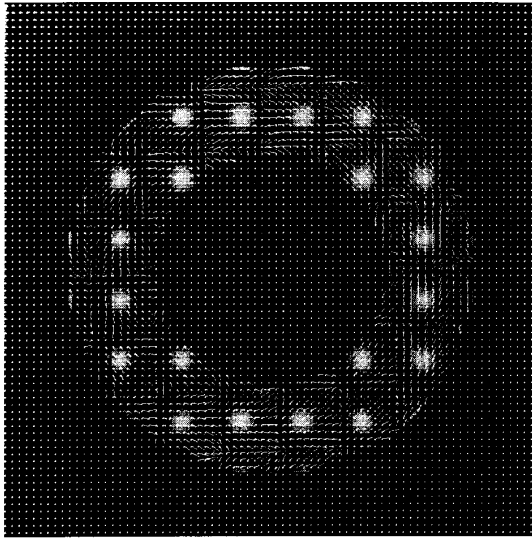
Fig. 6. Comparison of the performance of standard optical flow and variable brightness optical flow as a function of  $T_1$ .

pixel. Visually, it is clear that VBOF produces estimates that are generally consistent with our knowledge of the motion—a rotation—while SOF produces a somewhat chaotic appearing displacement field.

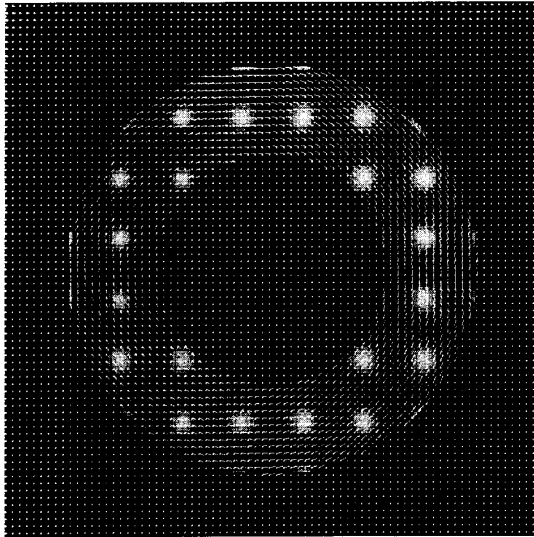
3) *Effect of Tag Spatial Frequency:* We now use a sequence of two images to measure the performance of variable brightness OF as a function of the tag pattern spatial frequency. As in our study of the tag modulation coefficient,  $T_1$  is made very large so that there is no difference between VBOF and SOF. Fig. 8 shows two image sequences of the simulated ring phantom tagged with different spatial frequency patterns. Fig. 9 shows the average percent velocity estimation error versus the rotation angle between images for the three different tag pattern spatial frequencies shown in Fig. 4, 8(a), and 8(b). Here we see an interesting behavior. At the smallest rotation angle, the tag pattern with the highest spatial frequency performs the best. As the rotation angle increases from its smallest value, the performance improves in all three cases. At a certain point the performance reaches its peak (minimum percent error) and degrades with higher rotation angles. In this range, however, the lower spatial frequency pattern achieves the best performance. The fact that at this point the performance degrades most rapidly with the higher spatial frequencies is indicative of an inherent ambiguity as the motion between frames is a large fraction of the period of the tag pattern. Therefore, the actual performance of VBOF—and, indeed, of SOF as well—depends on both the underlying size of the motion and the spatial frequency of the tag pattern. No precise expression relating the performance to the motion and spatial frequency of the tag pattern is known at present.

## B. Study 2: Motion-Tracking Performance

This simulation study involves tracking a set of images over time. We use the sequence of 10 images shown in Fig. 4 and compare three OF approaches: SOF, VBOF, and EVBOF. EVBOF, which stands for *exact* VBOF, uses exact knowledge of the reference map at each time step when calculating the material time derivative  $\dot{\psi}$  instead of using an



(a)



(b)

Fig. 7. Needle diagram overlaying the first of two images showing the displacement estimate for (a) SOF and (b) VBOF.

estimated reference map as in VBOF. Thus, EVBOF provides a measure of the increasing error incurred by VBOF due to errors in tracking alone. One can also think of EVBOF as being equivalent to SOF when there is no  $T_1$  decay, because, in this situation, the material time derivative is known (and is equal to zero). EVBOF, however, can never be used in practice since the material time derivative is only known exactly for the first image pair.

Fig. 10(a) shows the average percent velocity estimation error between pairs of images in the sequence. As expected, the best performance occurs with EVBOF. In fact, the performance of EVBOF improves with time, a consequence of the tag pattern becoming more favorable for gradient

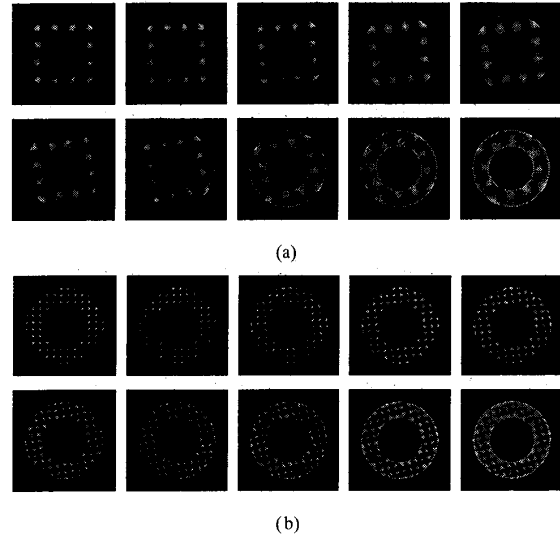


Fig. 8. Image sequences with (a)  $f_x = f_y = 0.5 \text{ cm}^{-1}$  and (b)  $f_x = f_y = 1.25 \text{ cm}^{-1}$ .

Error vs. Rotation

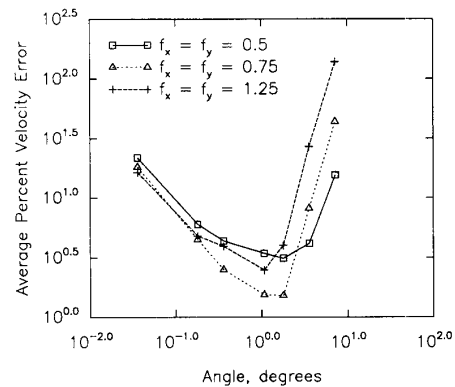


Fig. 9. Performance of variable brightness optical flow for different tag spatial frequencies as a function of the phantom rotation angle.

calculations (see Fig. 5). [Although this is not shown in the figure, ultimately as the tag pattern disappears, all gradient information will disappear and therefore the average percent error for all three methods will approach 100%.] The worst performance in Fig. 10(a) is achieved by SOF, although it too improves with time. SOF improves in time because the net difference in brightness between each successive pair of images decreases, effectively reducing the deleterious effects of  $T_1$  decay (see Fig. 6). Lying between these two extremes is VBOF, which achieves the same error between the first pair of images as EVBOF but develops reference map errors over time, leading to poorer performance. At a certain point (not shown in the figure), VBOF has worse performance than SOF, indicating that the reference map is no longer reliable.

For the same time series, Fig. 10(b) shows the tracking error over time for each of the three methods. Here, we

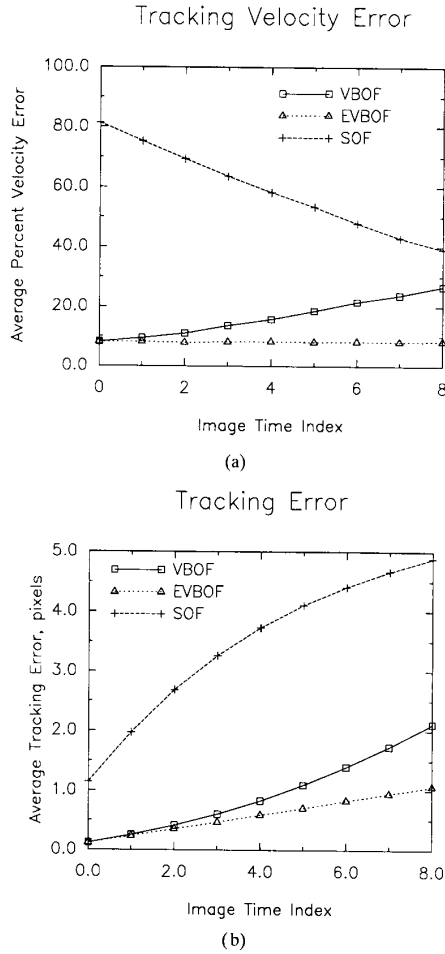


Fig. 10. (a) Optical flow performance and (b) average tracking error for the image sequence shown in Fig. 4 given different model assumptions.

use the estimated velocities computed by each method to determine the total motion over time. Since velocity is the derivative of displacement, the curves in Fig. 10(b) should be approximately equal to the integral of the corresponding curve in Fig. 10(a), which we see is approximately true. We see that even though the performance of VBOF degrades with time, the total tracking error over the entire image sequence is approximately one half that of SOF. This is because of the large errors incurred by SOF due to  $T_1$  decay at the beginning of the sequence.

Fig. 11 shows the first tagged image overlaid with path lines for various points as estimated by SOF and VBOF, representing motion through all ten images. We see that SOF generates path lines for the darker tagged regions that converge to the darkest point on the final image—and this is clearly in sharp disagreement with the true motion, which is a rotation. VBOF, in contrast, produces path lines which are more nearly representative of the true motion. The two superposed rays, which emanate from the center of the phantom indicate the total rotational motion of the phantom over the full image sequence. We see that SOF tends to overestimate the total

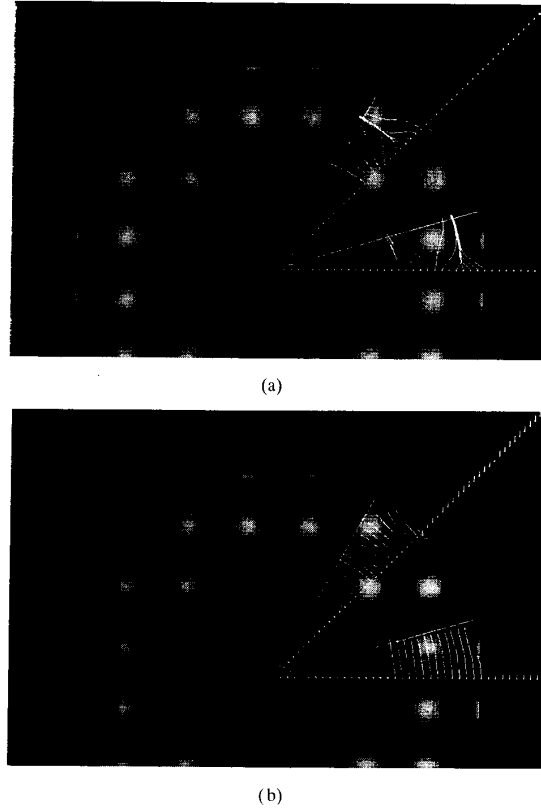


Fig. 11. The first tagged image of the image sequence in Fig. 4 is overlaid with various estimated path lines estimated using (a) SOF and (b) VBOF.

rotation while VBOF tends to underestimate the true total rotation. In preliminary investigations, we have shown that this bias is a function of both the tag pattern and the amount of motion. In particular, for small tag modulation coefficients, both SOF and VBOF will underestimate the total rotation; for larger tag modulation coefficients and small rotations, SOF will overestimate the total rotation while VBOF continues to underestimate it; and, finally, for both large tag modulation coefficients and large rotations, both SOF and VBOF will overestimate the total rotation. This problem may represent an inherent limitation to optical flow methods, but it deserves further investigation before drawing this conclusion.

### C. Study 3: Rotating Ring Phantom

For our experiments involving actual MR data, we used a gelatin "ring" phantom with the same dimensions as the simulated ring phantom. The gelatin within the ring has measured  $T_1 = 1.65$  s and  $T_2 = 0.9$  s and is surrounded by air; the phantom was rotated in the counterclockwise direction with frequency  $f_0 = 0.5$  rotations/s. A sequence of 10 tagged images, separated by 0.175 s, starting at  $t = 23$  ms was acquired and is shown in Fig. 12. The measured spatial frequencies are  $f_x = 1.117$  cm $^{-1}$  and  $f_y = 1.145$  cm $^{-1}$ .

Since the actual motion of the phantom is known, we were able to produce tracking error statistics for both SOF and



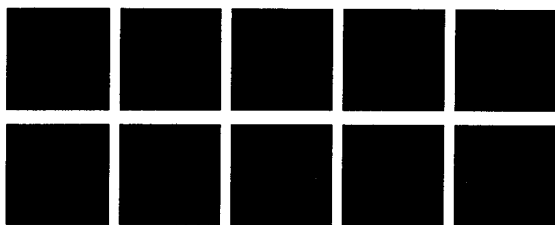


Fig. 12. Sequence of actual tagged images.

VBOF. As shown in Fig. 13(a), VBOF clearly outperforms SOF during the initial portion of the image sequence and produces correspondingly better tracking performance, as shown in Fig. 13(b). As VBOF develops tracking errors, however, its performance degrades to approximately the same level as SOF. The erratic behavior of both SOF and VBOF in Fig. 13(a) is due to motion artifacts appearing in the image sequence. Fig. 14 shows path lines for each method indicating an overall qualitative improvement with VBOF. Upon careful examination, however, one sees that while SOF causes dark pixels to converge to a point, in some cases VBOF is causing *bright* pixels to converge to a point. The reason for this is that the brightest pixels in the first image of this data set are fading slightly throughout the image sequence; this is in direct contradiction to our MR imaging equation, which causes an error in the calculation of the material time derivative at each time step. Hence, VBOF is overcompensating due to a modeling error.

The experimental results shown in Fig. 13 are qualitatively similar to the simulation results shown in Fig. 10; however, it is important to note that the spatial frequency of the tag pattern, the MR parameters, and the incremental angular rotation between images are different. (The simulations are more typical of the MR parameters and motion expected in the left ventricle.) Therefore, since the performance of both SOF and VBOF depend on these parameters (as shown in Figs. 5–9) we should expect numerical differences. Furthermore, the actual MR images contain noise due to additive Gaussian noise at the receiver and to motion artifacts, which degrades the performance of both SOF and VBOF. One feature that Fig. 13(b) shows which is absent in Fig. 10(b) is the degradation in tracking of VBOF to the point where SOF outperforms VBOF. This degradation is an important property of VBOF and must be considered in any application. It may, however, be possible to reduce the influence of reference map degradation by blending VBOF into SOF as the image sequence unfolds.

## V. CONCLUSION

We have presented a new optical flow algorithm called variable brightness optical flow (VBOF) for estimation of motion using MR imaging with tagging. We have shown that tagging can reduce the motion estimation errors caused by the aperture problem, and that variable brightness optical flow is markedly superior to standard optical flow on such tagged image sequences. We have also developed a simple method to

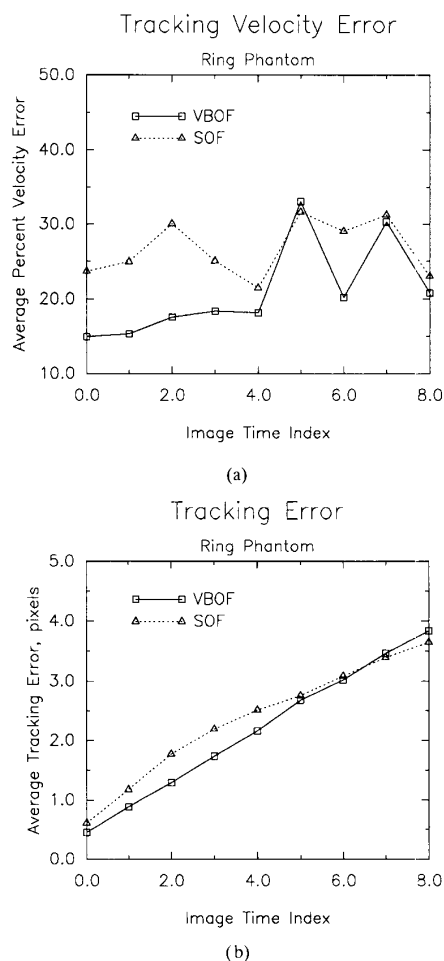


Fig. 13. (a) Optical flow performance and (b) average tracking error for the image sequence shown in Fig. 13 using SOF, VBOF, and EVBOF.

track both particle motion and the associated reference map, an essential step in the proper operation of VBOF over image sequences. Because of the dependency of VBOF on previous estimates of motion, its performance degrades with each new image; ultimately, standard OF outperforms VBOF. In the earliest images, however, average tracking error using VBOF is significantly smaller than the standard optical flow result. Moreover, the severe pathline convergence artifacts present when standard optical flow is used for tracking are virtually absent in the VBOF results.

Overall performance of VBOF is dependent upon many parameters of the imaging process including the natural brightness variations of the MR images themselves, the tag pattern imposed within these images, accurate knowledge of the initial MR parameters, the amount of motion, the observation noise, and the spatial and temporal sampling intervals. At present, there is no known relationship between these parameters and the overall motion estimation performance. This paper shows evidence, however, that given a specific motion the spatial frequency of the tag pattern strongly affects the performance.

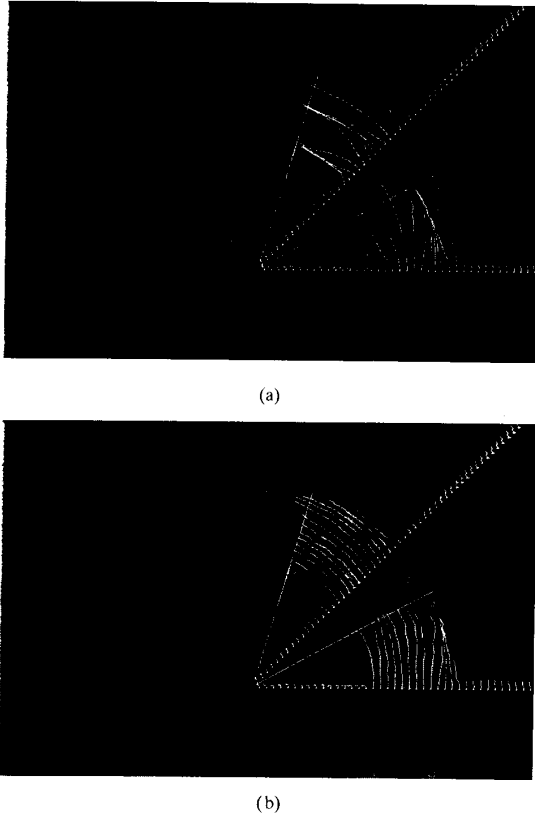


Fig. 14. The first tagged image from the MR phantom data is overlaid with various path lines estimated using (a) SOF and (b) VBOF.

We are confident that a tag pattern design principle which is based on having partial knowledge of the imaging parameters can be developed in the future.

## APPENDIX

### A. MR Imaging Equation

In this section we derive the imaging equation for MR tagged images. Throughout this section we assume that the motion is exactly periodic with period  $T_R$  and that a tag pulse-sequence and an imaging pulse-sequence, which reads one phase of a standard phase-encoded spin-echo image, are generated every period. We further assume that  $T_R \gg T_2$  everywhere in the sample, which guarantees that the transverse component of net magnetization component dies out between phase acquisitions. Assuming no tag pattern and  $T_R \gg T_1$ , the resultant image is given by<sup>3</sup>

$$\psi = D_0 e^{-T_E/T_2} \quad (19)$$

where  $T_E$  is the time between the  $90^\circ$  pulse and the spin echo in the imaging pulse-sequence. Since  $T_1 \gg T_R$  is not a good assumption in cardiac imaging, we must incorporate the fact that the spin system may not reach equilibrium before the

next imaging sequence begins. Again assuming no tag pattern is generated it is easily shown that

$$\psi = D_0 e^{-T_E/T_2} (1 - e^{-T_R/T_1}). \quad (20)$$

which is a standard result, and may be found in several texts (see, for example, [34]).

Now consider the effect of a tag pulse sequence generated at  $t = 0$  and assumed to be of negligible duration ( $\ll T_1$  or  $T_2$ ). This pulse-sequence tips the spins  $\theta$  radians off the  $z$ -axis and crushes the transverse magnetization (see Appendix B), yielding an effective spin density of

$$D'_0 = D_0 \cos \theta. \quad (21)$$

Since the imaging pulse-sequence is not initiated until after the delay time  $t = T_d$ , the spin-system has a chance to relax after the tag pulse, yielding another effective spin density

$$D''_0 = D_0 [1 + (\cos \theta - 1)e^{-T_d/T_1}] \quad (22)$$

at the time of the imaging pulse-sequence. Therefore, assuming  $T_R \gg T_1$  the tagged image is given by

$$\psi = D_0 e^{-T_E/T_2} [1 + (\cos \theta - 1)e^{-T_d/T_1}]. \quad (23)$$

As before, the case in which  $T_R \gg T_1$  is not a good assumption must be considered. Here, the spin-density just prior to the tag pulse-sequence is  $D_0(1 - e^{-(T_R - T_d)/T_1})$ . This spin is tipped by the tag pulse-sequence and crushed, which yields the image

$$\psi = D_0 e^{-T_E/T_2} \left\{ 1 + \left[ (1 - e^{-(T_R - T_d)/T_1}) \cos \theta - 1 \right] \cdot e^{-T_d/T_1} \right\}. \quad (24)$$

Adding and subtracting  $D_0 e^{-T_E/T_2} e^{-T_R/T_1}$  yields the imaging equation given in (1) and (2).

### B. Tag Pattern Generation

In this section we show how the tag pattern given in (16) can be generated. Let  $M(t) = [u(t)v(t)w(t)]^T$  denote the net magnetization at time  $t$  and  $M_0 = [u_0 v_0 w_0]^T$  denote the net magnetization at time  $t = 0$ . We assume that the tag pulse-sequence is generated rapidly, so that the effects of both longitudinal and transverse relaxation are negligible, and for convenience we sometimes drop the explicit time dependence in our notation.

The tag pulse-sequence begins at  $t = 0$  with an  $\alpha$ -degree pulse (taking duration  $\tau_\alpha$ ) about the  $y$ -axis, yielding net magnetization

$$M(\tau_\alpha) = \begin{bmatrix} \cos \alpha & 0 & \sin \alpha \\ 0 & 1 & 0 \\ -\sin \alpha & 0 & \cos \alpha \end{bmatrix} \begin{bmatrix} u_0 \\ v_0 \\ w_0 \end{bmatrix} \quad (25)$$

$$= \begin{bmatrix} u_0 \cos \alpha + w_0 \sin \alpha \\ v_0 \\ -u_0 \sin \alpha + w_0 \cos \alpha \end{bmatrix}. \quad (26)$$

Immediately after the initial  $\alpha$ -degree pulse, an  $x$ -gradient of strength  $G_x(t)$  and duration  $T_x$  is applied. For gradient pulses

<sup>3</sup>For notational convenience, we suppress the spatial dependency of all quantities in this and subsequent appendices.

of short duration, the solution to the Bloch equation is given to good approximation by

$$M(\tau_\alpha + T_x) = \begin{bmatrix} a \cos k_x x - v_0 \sin k_x x \\ a \sin k_x x + v_0 \cos k_x x \\ b \end{bmatrix} \quad (27)$$

where  $a = u_0 \cos \alpha + w_0 \sin \alpha$ ,  $b = -u_0 \sin \alpha + w_0 \cos \alpha$ , and  $k_x = 2\pi\gamma \int_0^{T_x} G_x(\tau) d\tau$  where  $\gamma$  is the gyromagnetic constant.

Next, a  $\beta$ -degree pulse taking duration  $\tau_\beta$  is applied, yielding

$$M(\tau_\alpha + \tau_\beta + T_x) = \begin{bmatrix} a \cos \beta \cos k_x x - v_0 \cos \beta \sin k_x x + b \sin \beta \\ a \sin k_x x + v_0 \cos k_x x \\ -a \cos \beta \cos k_x x + v_0 \sin \beta \sin k_x x + b \sin \beta \end{bmatrix}. \quad (28)$$

This equation is derived by using Equation (27) in place of the vector  $[u_0 v_0 w_0]^T$  in (25). A crusher pulse is immediately applied (taking duration  $T_c$ ), eliminating any effective transverse magnetization, leading to

$$M(\tau_\alpha + \tau_\beta + T_x + T_c) = \begin{bmatrix} \approx 0 \\ \approx 0 \\ -a \sin \beta \cos k_x x + v_0 \sin \beta \sin k_x x + b \cos \beta \end{bmatrix}. \quad (29)$$

Since crushers are used after imaging pulse-sequences (and we have made the assumption that  $T_R \gg T_2$ ) it is safe to assume that  $u_0 = v_0 = 0$ . Therefore, upon substitution for  $a$  and  $b$ , the  $z$ -magnetization may now be written

$$w(\tau_\alpha + \tau_\beta + T_x + T_c) = w_0(\cos \alpha \cos \beta - \sin \alpha \sin \beta \cos k_x x). \quad (30)$$

To generate the tag pattern in the  $y$ -direction, a sequence of events identical to that given above follows at this point, with the exception that a  $y$ -gradient of strength  $G_y(t)$  and duration  $T_y$  is applied between the  $\alpha$ -degree and  $\beta$ -degree pulses. Since a crusher is used after the  $x$ -gradient sequence (and since both sequences are assumed to be much faster than both  $T_2$  and  $T_1$ ), we find that the net magnetization after the two sequences, including the trailing crusher, is just the  $z$ -magnetization component, which is given by

$$w(2\tau_\alpha + 2\tau_\beta + 2T_c + T_x + T_y) = w_0(\cos \alpha \cos \beta - \sin \alpha \sin \beta \cos k_y y) \cdot (\cos \alpha \cos \beta - \sin \alpha \sin \beta \cos k_y y) \quad (31)$$

where  $k_y = 2\pi\gamma \int_0^{T_y} G_y(\tau) d\tau$ . Letting  $\alpha = \beta = \theta$  and setting  $p_x = x$  and  $p_y = y$ , the spatial tag pattern of (16) results.

### C. Numerical Methods

To solve the coupled Poisson equations of (7a) and (7b), we implement the local relaxation algorithm described by Kuo *et al.* [33], also implemented for optical flow by Rougee, *et al.* [32]. The domain is a rectilinear lattice with  $n_x$  pixels in the horizontal direction and  $n_y$  pixels in the vertical direction and

with vertical and horizontal sample spacings of  $h_x$  and  $h_y$ , respectively. Then, indexing the pixels by  $i$  and  $j$  for horizontal and vertical, respectively, the coupled PDE's may be solved numerically by iteration first on the red points ( $i+j$ ) even and then on the black points ( $i+j$ ) odd, and repeating until a convergence criterion is satisfied. The iterations are given by the following.

*Red points ( $i+j$  even):*

$$u_{i,j}^{(n+1)} = (1 - \omega_{i,j}^x) u_{i,j}^{(n)} + \omega_{i,j}^x \left( u_{i-1,j}^{(n)} + u_{i+1,j}^{(n)} + u_{i,j-1}^{(n)} + u_{i,j+1}^{(n)} - \frac{h_x^2}{\alpha^2} \psi_x [\psi_y v_{i,j}^{(n)} - \psi_t + \psi] \right) / d_{i,j}^x \quad (32a)$$

$$v_{i,j}^{(n+1)} = (1 - \omega_{i,j}^y) v_{i,j}^{(n)} + \omega_{i,j}^y \left( v_{i-1,j}^{(n)} + v_{i+1,j}^{(n)} + v_{i,j-1}^{(n)} + v_{i,j+1}^{(n)} - \frac{h_y^2}{\alpha^2} \psi_y [\psi_x u_{i,j}^{(n+1)} - \psi_t + \psi] \right) / d_{i,j}^y. \quad (32b)$$

*Black points ( $i+j$  odd):*

$$u_{i,j}^{(n+1)} = (1 - \omega_{i,j}^x) u_{i,j}^{(n)} + \omega_{i,j}^x \left( u_{i-1,j}^{(n+1)} + u_{i+1,j}^{(n+1)} + u_{i,j-1}^{(n+1)} + u_{i,j+1}^{(n+1)} - \frac{h_x^2}{\alpha^2} \psi_x [\psi_y v_{i,j}^{(n+1)} - \psi_t + \psi] \right) / d_{i,j}^x \quad (33a)$$

$$v_{i,j}^{(n+1)} = (1 - \omega_{i,j}^y) v_{i,j}^{(n)} + \omega_{i,j}^y \left( v_{i-1,j}^{(n+1)} + v_{i+1,j}^{(n+1)} + v_{i,j-1}^{(n+1)} + v_{i,j+1}^{(n+1)} - \frac{h_y^2}{\alpha^2} \psi_y [\psi_x u_{i,j}^{(n+1)} - \psi_t + \psi] \right) / d_{i,j}^y. \quad (33b)$$

Here, the coefficients  $d_{i,j}^x$  and  $d_{i,j}^y$  are given by

$$d_{i,j}^x = 4 + \psi_x^2 h_x^2 / \alpha^2 \quad (34a)$$

$$d_{i,j}^y = 4 + \psi_y^2 h_y^2 / \alpha^2 \quad (34b)$$

and  $\omega_{i,j}^x$  and  $\omega_{i,j}^y$  are called the *local relaxation parameters* and are given by

$$\omega_{i,j}^x = \frac{2}{1 + \sqrt{1 - (\rho_{i,j}^x)^2}}, \quad (35a)$$

$$\omega_{i,j}^y = \frac{2}{1 + \sqrt{1 - (\rho_{i,j}^y)^2}} \quad (35b)$$

where

$$\rho_{i,j}^x = \frac{2}{d_{i,j}^x} \left( \cos \frac{\pi}{n_x + 1} + \cos \frac{\pi}{n_y + 1} \right), \quad (36a)$$

$$\rho_{i,j}^y = \frac{2}{d_{i,j}^y} \left( \cos \frac{\pi}{n_x + 1} + \cos \frac{\pi}{n_y + 1} \right). \quad (36b)$$

The terms  $\psi_x$ ,  $\psi_y$ , and  $\psi_t$  in (32a), (32b), (33a), and (33b) are evaluated at pixel  $i, j$  and are calculated using the following local approximations:

$$\psi_x = (z_4 + z_9 - z_2 - z_7)/4h_x \quad (37)$$

$$\psi_y = (z_1 + z_6 - z_5 - z_{10})/4h_y \quad (38)$$

$$\psi_t = (z_6 + z_7 + z_8 + z_9 + z_{10} - z_1 - z_2 - z_3 - z_4 - z_5)/5\tau \quad (39)$$

where

$$z_1 = \psi_{i-1,j}(t) \quad (40)$$

$$z_2 = \psi_{i,j-1}(t) \quad (41)$$

$$z_3 = \psi_{i,j}(t) \quad (42)$$

$$z_4 = \psi_{i,j+1}(t) \quad (43)$$

$$z_5 = \psi_{i+1,j}(t) \quad (44)$$

$$z_6 = \psi_{i-1,j}(t + \tau) \quad (45)$$

$$z_7 = \psi_{i,j-1}(t + \tau) \quad (46)$$

$$z_8 = \psi_{i,j}(t + \tau) \quad (47)$$

$$z_9 = \psi_{i,j+1}(t + \tau) \quad (48)$$

$$z_{10} = \psi_{i+1,j}(t + \tau). \quad (49)$$

#### ACKNOWLEDGMENT

The authors wish to thank Dr. E. Zerhouni for his guidance throughout the course of this research, and Mr. B. Bolster for programming the tag pattern pulse-sequences and assistance in acquiring data.

#### REFERENCES

- [1] A. N. Lieberman *et al.*, "Two-dimensional echocardiography and infarct size: Relationship of regional wall motion and thickening to the extent of myocardial infarction in the dog," *Circulation*, vol. 63, p. 739, 1981.
- [2] A. J. Buda, R. J. Zotz, and K. P. Gallagher, "Characterization of the functional border zone around regionally ischemic myocardium using circumferential flow-function maps," *J. Amer. Coll. Cardiol.*, vol. 9, p. 150, 1986.
- [3] J. A. C. Lima *et al.*, "Impaired thickening of nonischemic myocardium during acute regional ischemia in the dog," *Circulation*, p. 1048, 1985.
- [4] W. C. Hunter and E. A. Zerhouni, "Imaging distinct points in left ventricular myocardium to study regional wall deformation," in *Innovations in Diagnostic Radiology*. Berlin: Springer-Verlag, 1989.
- [5] K. L. Gould *et al.*, "Analysis of wall dynamics and directional components of left ventricular contraction in man," *Amer. J. Cardiol.*, vol. 38, p. 322, 1976.
- [6] T. Arts, S. Meerbaum, and R. S. Reneman, "Torsion of the left ventricle during the ejection phase in the intact dog," *Cardiovasc. Res.*, vol. 18, p. 183, 1984.
- [7] C. H. Chu, E. J. Delp, and A. J. Buda, "Detecting left ventricular endocardial and epicardial boundaries by digital two-dimensional echocardiography," *IEEE Trans. Med. Imaging*, vol. 7, June 1986.
- [8] N. Friedland and D. Adam, "Automatic ventricular cavity boundary detection from sequential ultrasound images using simulated annealing," *IEEE Trans. Med. Imaging*, vol. 8, Dec. 1989.
- [9] E. R. Wolfe, E. J. Delp, C. R. Meyer, F. L. Bookstein, and A. J. Buda, "Accuracy of automatically determined borders in digital two-dimensional echocardiography using a cardiac phantom," *IEEE Trans. Med. Imaging*, vol. MI-6 Dec. 1987.
- [10] D. Adam, O. Hareuveni, and S. Sideman, "Semiautomated border tracking of cine echocardiographic ventricular images," *IEEE Trans. Med. Imaging*, vol. MI-6 Sept. 1987.
- [11] G. E. Mailloux, F. Langlois, P. Y. Simard, and M. Bertrand, "Restoration of the velocity field of the heart from two-dimensional echocardiograms," *IEEE Trans. Med. Imaging*, vol. 8, pp. 143-153, 1989.
- [12] D. P. Boyd and M. J. Lipton, "Cardiac computed tomography," *Proc. IEEE*, vol. 71, Mar. 1983.
- [13] I. G. McDonald, "The shape and movements of the human left ventricle during systole," *Amer. J. Cardiol.*, vol. 26, p. 221, 1970.
- [14] N. B. Ingels *et al.*, "Evaluation of methods for quantitating left ventricular segmental wall motion in man using myocardial markers as a standard," *Circulation*, vol. 61, p. 966, 1980.
- [15] J. H. Myers, M. C. Stirling, M. Choy, A. J. Buda, and K. P. Gallagher, "Direct measurement of inner and outer wall thickening dynamics with epicardial echocardiography," *Circulation*, vol. 74, p. 164, 1986.
- [16] G. Osakada *et al.*, "The analysis of left ventricular wall thickness and shear by ultrasonic triangulation technique in the dog," *Circ. Res.*, vol. 47, p. 173, 1980.
- [17] P. R. Moran, "A flow velocity zeugmatographic interlace for NMR imaging in humans," *Magnet. Res. Imaging*, vol. 1, pp. 197-201, 1982.
- [18] N. J. Pelc, A. Shimakawa, and G. H. Glover, "Phase contrast cine MRI," in *Proc. Soc. Magnet Res. Med.*, p. 101, Soc. Mag. Res. Med., 1989. Annu. Meet., abstract only.
- [19] E. A. Zerhouni, D. M. Parish, W. J. Rogers, A. Yang, and E. P. Shapiro, "Human heart: Tagging with MR imaging—A method for noninvasive assessment of myocardial motion," *Radiology*, vol. 169, pp. 59-63, 1988.
- [20] L. Axel and L. Dougherty, "MR imaging of motion with spatial modulation of magnetization," *Radiology*, vol. 171, pp. 841-845, 1989.
- [21] —, "Heart wall motion: Improved method of spatial modulation of magnetization for MR imaging," *Radiology*, vol. 172, p. 349, 1989.
- [22] M. A. Guttman and J. L. Prince, "Image analysis methods for tagged MRI cardiac studies," in *Medical Imaging IV: Image Processing*. Bellingham, WA: SPIE, 1990.
- [23] E. R. McVeigh and E. A. Zerhouni, "Non-invasive measurement of transmural gradients in myocardial strain with magnetic resonance imaging," *Radiology*, vol. 180, no. 3 pp. 677-683, 1991.
- [24] B. K. P. Horn and B. G. Schunck, "Determining optical flow," *Artificial Intell.*, vol. 17, pp. 185-203, 1981.
- [25] E. C. Hildreth, *Measurement of Visual Motion*. MA: M.I.T. Press Cambridge, 1984.
- [26] S. M. Song and R. M. Leahy, "Computation of 3-D velocity fields from 3-D cine CT images of a human heart," *IEEE Trans. Med. Imaging*, vol. 10, pp. 295-306, Sept. 1991.
- [27] J. L. Prince, "Reducing the aperture effect by object tagging in MR imaging," in *Proc. 1990 Conf. Inform. Sci. Sys.*, Princeton Univ., 1990.
- [28] —, "Cardiac motion estimation from MR image sequences," in *Proc. SPIE's Int. Symp. Opt. Optoelect. Appl. Sci. Eng.: Mathematical Imaging*. Bellingham, WA: SPIE, 1990.
- [29] J. L. Prince and E. R. McVeigh, "Optical flow for tagged MR images," in *Proc. 1991 Int. Conf. Acoust., Speech, Signal Processing*, 1991, pp. 2441-2444. IEEE Catalog No. 91CH2977-7.
- [30] M. E. Gurtin, *An Introduction to Continuum Mechanics*. New York: Academic, 1981.
- [31] W. S. Hinshaw and A. H. Lent, "An introduction to NMR imaging: From the Bloch equation to the imaging equation," *Proc. IEEE*, vol. 71, pp. 338-350, 1983.
- [32] A. Rougee, B. C. Levy, and A. S. Willsky, "Optic flow estimation inside a bounded domain," M.I.T. Lab. Inform. and Decision Syst., Tech. Rep. LIDS-P-1589, 1986.
- [33] C.-C. J. Kuo, B. C. Levy, and B. R. Mucic, "A local relaxation method for solving elliptic PDE's on mesh-connected arrays," *SIAM J. Sci. Stat. Comput.*, vol. 8, no. 4, pp. 550-573, 1987.
- [34] S. L. Thomas and R. L. Dixon, Eds., *NMR in Medicine: The Instrumentation and Clinical Applications*. American Institute of Physics, 1986. American Assoc. of Physicists, Medical Physics Monograph 14.